Icarus 285 (2017) 211–223

Contents lists available at ScienceDirect

Icarus

journal homepage: www.elsevier.com/locate/icarus

High energy electron sintering of icy regoliths: Formation of the PacMan thermal anomalies on the icy Saturnian moons

M.J. Schaible[a,*], R.E. Johnson[a], L.V. Zhigilei[a], S. Piqueux[b]

[a] Dept. of Materials Science and Engineering, University of Virginia, Charlottesville, VA, United States
[b] Jet Propulsion Laboratory, California Institute of Techonology, Pasadena, CA, United States

ARTICLE INFO

Article history:
Available online 6 September 2016

ABSTRACT

The so-called 'PacMan' features on the leading hemispheres of the icy Saturnian moons of Mimas, Tethys and Dione were initially identified as anomalous optical discolorations and subsequently shown to have greater thermal inertia than the surrounding regions. The shape of these regions matches calculated deposition contours of high energy plasma electrons moving opposite to the moon's orbital direction, thus suggesting that electron interactions with the grains produce the observed anomalies. Here, descriptions of radiation-induced diffusion processes are given, and various sintering models are considered to calculate the rate of increase in the contact volume between grains in an icy regolith. Estimates of the characteristic sintering timescale, i.e. the time necessary for the thermal inertia to increase from that measured outside the anomalous regions to that within, are given for each of the moons. Since interplanetary dust particle (IDP) impact gardening and E-ring grain infall would be expected to mix the regolith and obscure the effects of high energy electrons, sintering rates are compared to rough estimates of the impact-induced resurfacing rates. Estimates of the sintering timescale determined by extrapolating laboratory measurements are below ~0.03 Myr, while the regolith renewal timescales are larger than ~0.1 Myr, thus indicating that irradiation by the high energy electrons should be sufficient to form stable thermal anomalies. More detailed models developed for sintering of spherical grains are able to account for the radiation-induced anomalies on Mimas and Tethys only if the regoliths on those bodies are relatively compact and composed of small ($\lesssim 5\,\mu m$) grains or grain aggregates, and/or the grains are highly non-spherical with surface defect densities in the inter-grain contact regions that are much higher than expected for crystalline water ice grains at thermal equilibrium. These results are consistent with regolith thermal conductivity models which can only be reconciled with spacecraft observations if the contacts between grains are assumed to have much lower thermal conductance than predicted for idealized grains. The strength of the anomalies on Tethys and Dione appear to be limited by E-ring grain infall, while on Mimas IDP gardening limits the strength of the anomaly. The smaller flux of more deeply penetrating high energy (>1 MeV) electrons on Dione can account for the small thermal inertia differences measured there. Determining regolith sintering rates and the corresponding effect on thermal conductivity can, in principle, provide an independent constraint on the regolith grain geometries and exposure timescales for icy bodies.

1. Introduction

Anomalous weathering features have been identified on the icy Saturnian moons Mimas, Tethys, and Dione. First identified during the Voyager era as a dark equatorial band in visible light images of Tethys (Buratti et al., 1990; Stooke, 1989; 2002), more recent images from the Imaging Science Subsystem (ISS) on Cassini clearly show near-UV (0.338 μm) brightening and NIR (0.930 μm) darkening of Mimas and Tethys in regions centered on the leading hemisphere and roughly symmetric about the equator (Elder et al., 2007; Schenk et al., 2011). Additionally, the Cassini InfraRed Spectrometer (CIRS) measurements of thermal emission in the mid-IR regime (9.1 – 16.7 μm) revealed that temperature variations during a diurnal cycle were smaller in the anomalous regions on all three bodies (Howett et al., 2012; 2014; 2011), indicating larger thermal inertias. The shape within the CIRS daytime temperature maps, reproduced in Fig. 1, led to the anomalies becoming colloquially known as the 'PacMac' features. The spatial boundaries of the optical and thermal anomalies were similar, suggesting a common origin. However, reflectance features were not seen in the far-UV data (170 – 190 nm) taken by the Ultraviolet Imaging Spectrometer

* Corresponding author.
E-mail address: ms5vf@virginia.edu (M.J. Schaible).

http://dx.doi.org/10.1016/j.icarus.2016.08.033
0019-1035/

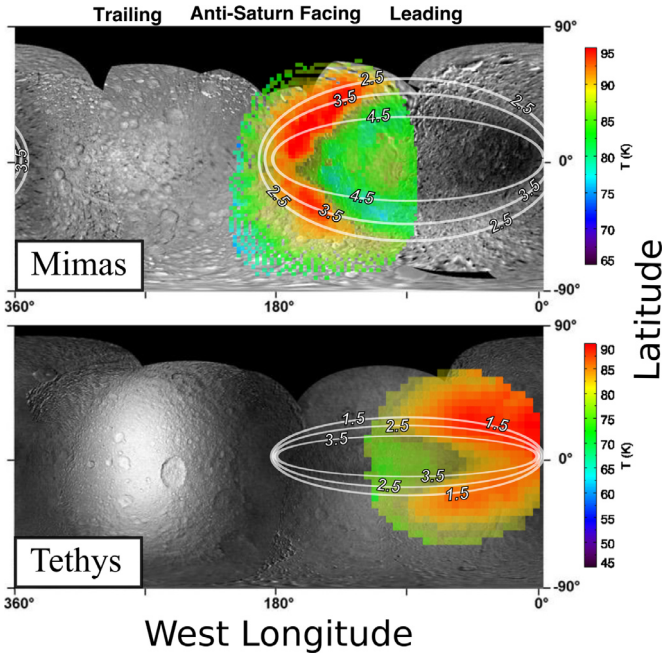

Fig. 1. The panels show the anomalous 'PacMan' features identified on the leading hemispheres of Mimas and Tethys. Energy flux contours, given in units of log_{10}(MeV/cm^2/s) (Paranicas et al., 2012), superimposed on the IR/UV ratio maps (Schenk et al., 2011) appear to match the shape of the anomalous regions. The daytime surface temperatures for each of the bodies are given as color maps (Howett et al., 2012; 2011) and clearly show lower daytime temperatures (corresponding to higher thermal inertia) inside the anomalous regions with boundaries roughly consistent with the discolorations. (For interpretation of the references to color in this figure legend, the reader is referred to the web version of this article.)

(UVIS) (Hendrix et al., 2012) or in the mid-IR (0.8 – 5.1 μm) wavelengths (Scipioni and Schenk, 2014). This absence was explained by different sampling depths of the spectral data sets and different regolith properties as a function of depth.

That the moons are embedded in the energetic Saturnian magnetospheric plasma suggests the anomalies are produced by plasma interactions with the water ice grains that compose the regolith. The moons are tidally locked and deposition of the faster rotating thermal plasma occurs preferentially on the trailing hemispheres with the ions penetrating the regolith to ~μm depths and the electrons up to ~mm. In addition to orbital motion, the plasma particles 'bounce' along magnetic field lines perpendicular to the orbital plane. For electrons with energies above ~10 keV, the lateral drift during half a bounce period is less than the diameter of the moons, and it can be assumed that whenever the electron path crosses a body the electron is absorbed on the surface. At electron energies above the co-rotational resonance energy, $\mathcal{E}_{cr}$, the gradient and curvature drifts are strong enough to cause electrons to move in a rotational direction opposite to that of the moons and the thermal plasma (Paranicas et al., 2012; Roussos et al., 2007). These electrons impact preferentially on the leading hemisphere and penetrate the regolith up to cm depths. The resulting deposition pattern is distinctly lens shaped as seen in Fig. 1. The measured thermal and electron properties for the icy moons, as well as published estimates for the average regolith grain radii determined from reflectance measurementsl, are given in Table 1.

Using electron energy spectra measured by the Low Energy Magnetospheric Measurements System (LEMMS) on the Cassini Magnetosphere Imaging Instrument (MIMI) (Krimigis et al., 2004) in the vicinity of the moons, the expected deposition profiles for electrons with energies above $\mathcal{E}_{cr}$ were shown to closely match the shape and location of the anomalies as seen in Fig. 1. The boundaries of the thermal anomalies were fit by an energy deposition flux of 5.6 × 10^4 MeV/(cm^{2}s) at Mimas and 1.8 × 10^4 MeV/(cm^{2}s) at Tethys (Howett et al., 2012; 2011). The thermal inertia differences are much weaker on Dione and it is difficult to fit a specific energy flux contour to the anomaly boundary. Therefore, that of Tethys is assumed here. Furthermore, the skin depths of the thermal anomalies, δ, given in Table 1, and the estimated penetration depth of the MeV electrons are both on the order of a centimeter. The combination of these results provides strong support for the hypothesis that high energy electrons are responsible for the increased thermal inertia in the anomalous regions. Similar weathering features due to trapped magnetospheric plasma have also been identified on Europa (Paranicas et al., 2001).

Despite the apparent correlations, the physical mechanisms by which the electrons drive changes in surface reflectance and thermal inertia have not been fully described and a quantitative comparison with theoretical and experimental results is lacking. One proposed mechanism for the increase in thermal inertia was growth or annealing of grain contacts resulting from high energy electron interactions with the ice. The process of atoms or molecules migrating into the contact region between grains due to thermal or radiation-induced diffusion is called sintering and is well studied in materials processing (e.g., ceramics). The electron interactions can also anneal highly amorphous grains, producing crystalline regions with residual defects, and rearrange the molecular bonding at the interface between grains, directly annealing the ice in the contact region. The transformation of ice from amorphous to crystalline can increase thermal conductivity. However, for reasonable assumptions of crystalline fraction in the ice grains and the thermal conductivities of amorphous and crystalline ice, the crystallization of amorphous grains is insufficient to account for the measured differences, thus implying that the higher thermal inertia results primarily from changes in the size and morphology of the contact regions between grains.

Assuming that, initially, thermal transport between grains is inefficient due to poorly bonded or small contacts between grains, interactions that occur near the contact region will cause molcules to accumulate and 'cement' or sinter the region between grains. Molecules preferentially collect on the periphery of the contact region where the curvature is the largest and surface energy is a minimum. Sintering improves the ability of the contact to conduct heat between grains and, consequently, increases the effective thermal inertia of the regolith. However, due to the expected roughness of regolith grains, the possibility of small amounts of amorphous ice and salt or organic inclusions, and the cold surface temperatures of the Saturnian moons (~ 60 – 90 K at Mimas), the application of thermal conductivity and sintering models developed using simplifying assumptions for the grain shape and material behavior is not straightforward.

In this paper, we start by providing a brief overview of various thermal conductivity models for granular, porous regoliths in Section 2, and use a simple model to estimate the grain contact radii implied by the CIRS thermal inertia measurements. Electron interactions with water ice are then described in Section 3 and Monte Carlo calculations are used to determine the energy deposition rate and penetration depth of electrons into an amorphous water target. A sintering model based on experimental measurements of radiation-induced compaction of porous water ices is presented Section 4 and used to estimate timescales for the contact region to grow sufficiently to explain the thermal inertia differences inside and outside the anomalous regions. Meteoroid impacts and E-ring grain infall will both melt and redistribute material across the surface, refreshing the exposed surface and obscuring the sintering effects produced by the MeV electrons. If indeed the MeV electrons are responsible for the thermal anomalies, the regolith renewal timescale should be comparable to or longer than

Table 1
Measured thermal properties inside and outside the anomalies (Howett et al., 2012; 2014; 2011), grain sizes (Filacchione et al., 2010; Hendrix et al., 2012), and high energy electron fluxes (Paranicas et al., 2012) at the icy Saturnian Moons. The thermal skin depth is defined as $\delta = \frac{I}{\rho_{ice}(1-\phi)c_{ice}\sqrt{\omega}}$, where $\phi = 50\%$ is the assumed porosity, ω is the angular velocity of rotation of each moon and $c_{ice} \sim 12.4$ J/(mol K) and $\rho_{ice} \sim 0.94$ g/cm^3 are, respectively, the heat capacity and density of crystalline ice at 80 K.

Body	Thermal inertia I $\left[\frac{J}{m^2 s^{1/2} K}\right]$	Skin depth δ [cm]	Grain radius r_g [μm]	Co-rotational resonance energy, $\mathcal{E}_{cr}$ [MeV]	Electron flux Φ_{elec} [elec/cm^2/s]
Mimas					
In	66 ± 23	2.01 ± 0.7	10 – 40	~1.04	~1.45×10^4
Out	<16	<0.49	5 – 25		
Tethys					
In	25 ± 3	0.76 ± 0.09	~35	~0.84	~1.18×10^4
Out	5 ± 1	0.15 ± 0.03			
Dione					
Leading	11	0.57	~30	~0.63	~1.68×10^4
Trailing	8	0.42			

the grain sintering timescale at depths shallower than the thermal skin depth. A full radiation-induced sintering model depending on grain size and shape is proposed in Section 5, and results are used to constrain regolith grain properties and surface ages.

2. Thermal conductivity of a porous, granular regolith

The plumes of water ice particles from Enceladus are thought to produce the bulk of the ~ μm sized E-ring grains (Dougherty et al., 2006; Porco et al., 2006; Spahn et al., 2006b), although impacts of the E-ring grains and interplanetary dust particles (IDPs) onto the icy moon surfaces may also contribute (Juhász and Horányi, 2002; Spahn et al., 2006a). The E-ring grains have relatively low impact velocities (~5 km/s at Tethys) and likely sandblast the surface grains (Verbiscer et al., 2007), with most of the disturbed material returning to the regolith and depositing fresh ice on the grains. The IDPs penetrate more deeply and cause more extensive melting and mixing of regolith materials (Kirchoff and Schenk, 2009; Porter et al., 2010). Here we assume that thermal conductivity is a minimum for a surface that has recently been struck by an IDP or E-ring grain.

The measured thermal inertia, I, is related to effective thermal conductivity of the regolith, k_{eff}, by $I = \sqrt{k_{eff} c_{ice} \rho_{reg}}$ where c_{ice} is the heat capacity of ice, and $\rho_{reg} = \rho_{ice}(1-\phi)$ is the density and ϕ the porosity of the regolith. For airless bodies in the outer solar system, contributions to thermal conductivity other than solid state conduction (i.e., radiative, convective, and latent heat) can be shown to be negligible. Heat flow is then determined by the number of contacts between grains and the 'quality' or size of the contacts (e.g., Wood, 2013a,b; Gundlach and Blum, 2012; Sirono and Yamamoto, 1997), and k_{eff} will increase as the effective contact radius, R_{con}, increases. The effective contact radius is the equivalent contact radius for spherical grains and can increase either by addition of cementation material or annealing of the ice. In order to get an idea of the contact size difference necessary to explain the thermal conductivity differences inside and outside the anomalous regions, we first consider standard thermal conductivity models for granular regoliths.

A typical idealized contact between spherical grains of thermal conductivity k_g cemented together by a material with thermal conductivity k_{cem} is shown in Fig. 2. Using this model of the contact region and assuming $R_{con} \ll r_g$, the cementation volume fraction, χ, for a grain in contact with N_c neighbors is related to R_{con}/r_g by

$$\chi = \frac{V_{cem}}{V_g} \approx \frac{3}{16} N_c \left(\frac{R_{con}}{r_g}\right)^4 \quad (1)$$

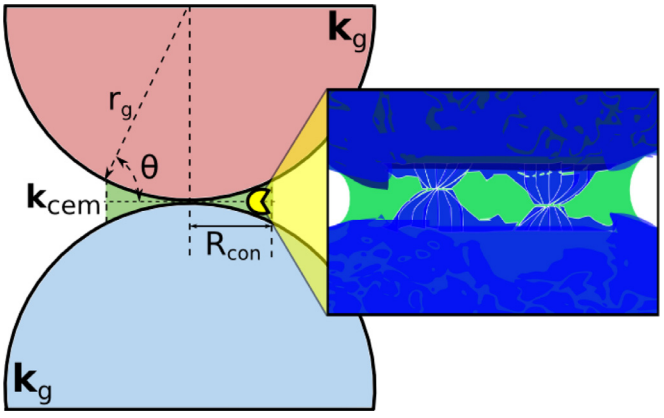

Fig. 2. A simple model for spherical grains of radius r_g with a distinct cementation phase filling the contact region. The effective thermal conductivity of this system depends on the contact radius, R_{con}, and the thermal conductivities of the cementation phase, k_{cem}, and grain, k_g. The inset shows a more realistic representation of a contact region between two rough grains (blue) that has been sintered such that cementation (green) filled the contact region, thus increasing the thermal conductance between grains. (For interpretation of the references to color in this figure legend, the reader is referred to the web version of this article.)

where V_g and V_{cem} are the grain volume and the average cementation volume per grain, respectively. Eq. (1) assumes that cementation fills the neck region between the grains symmetrically and that the surface of the neck has zero curvature. For spherical grains, an effective minimum contact radius, R_{Hertz}, can be estimated from Hertzian contact theory as shown in Appendix A. For ~ μm sized, uncemented, spherical Ih water ice grains at 80 K and zero external pressure, $R_{Hertz} \sim 0.01 r_g$. The number of neighbor contacts $N_c = 6$ for simple cubic packing arrangements of monodisperse spheres. Although in a real regolith R_{con} depends on the sizes and shapes of the grains and may change with depth below the surface, the precise range of these parameters has not yet been determined from spacecraft imagery of the icy satellites.

Models developed to simulate heat transport in planetary and cometary surfaces and in 'packed-beds' of grains typically assume idealized grain shapes and packing arrangements (Chan and Tien, 1973; Piqueux and Christensen, 2009), or use a combination of analytical theory and fitting to experimental data to determine parameterized equations accounting for grain size, shape and packing (Gundlach and Blum, 2012). One such simple model is (Sirono and Yamamoto, 1997)

$$k_{eff} = \frac{\pi k_g}{g}\left(\frac{p - p_c}{1 - p_c}\right)\left(\frac{R_{con}}{r_g}\right)^2 \quad (2)$$

Table 2
Effective contact radius to grain radius ratios (R_{con}/r_g) inside and outside the anomalies calculated using the Sirono and Yamamoto (1997) regolith thermal conductivity model for an average regolith temperature of 80 K. The porosities and grain thermal conductivities assumed are within the range of reasonable values expected for icy regoliths, and the error bounds are due to uncertainty in the thermal inertia measurements. For comparison, the contact ratio predicted from Hertzian contact theory for spherical water ice grains is $R_{Hertz}/r_g = 0.011$ where the mechanical properties for low temperature ice (<100 K) were taken from Hobbs (1974).

R_{con}/r_g	$\phi = 0.5$ $k_g = 6.5$ W/m/K	$\phi = 0.65$ $k_g = 6.5$ W/m/K	$\phi = 0.5$ $k_g = 0.5$ W/m/K
Mimas			
In	0.026 ± 0.001	0.037 ± 0.003	0.089 ± 0.033
Out	~0.01	~0.01	~0.02
Tethys			
In	0.010 ± 0.001	0.014 ± 0.002	0.033 ± 0.004
Out	0.002 ± 0.001	0.003 ± 0.001	0.007 ± 0.001
Dione			
Leading	0.004 ± 0.002	0.006 ± 0.002	0.015 ± 0.005
Trailing	0.003 ± 0.001	0.005 ± 0.002	0.011 ± 0.001

where r_g is the grain radius and $g \sim 1$ is a geometrical factor dependent on the packing structure (Ferrari and Reffet, 2013). The packing fraction, p, is related to the porosity by

$$p = \left(\frac{6}{\pi}\right)(1-\phi)$$

and the critical packing fraction $p_c = 1/3$ is the minimum necessary for a continuous thermal path. This model does not distinguish between the grain and cementation materials and assumes that the conductivity of the void space is zero. Using the measured thermal inertias in Table 1, the ratios R_{con}/r_g estimated from Eq. (2) are given in Table 2 where several values of porosity and grain thermal conductivity were considered due to uncertainty in the actual regolith parameters (Filacchione et al., 2010; Hendrix et al., 2012). It is seen that inside the anomalous regions R_{con}/r_g is of the order of the Hertzian contact ratio, while outside the anomalous regions this ratio can be much smaller. This suggests that spherical grains are only a crude approximation. The R_{con}/r_g is the largest for the Mimas thermal anomaly, thus impying that grain sintering is more efficient and/or resurfacing processes are less efficient than on Tethys and Dione. As described further below, grain sintering rates are dependent on the grain and contact sizes, and the values from Table 2 are used for defining the limiting (maximum and minimum) values in the calculation of the grain sintering timescales.

Due to the dependence of R_{con} and ϕ on r_g, the precise relationship between r_g and k_{eff} is more complicated than suggested by Eq. (2) (Presley and Christensen, 1997). Although somewhat different grain size distributions (Hendrix et al., 2012) and small porosity differences (Annex et al., 2013; Verbiscer et al., 2014) have been measured inside and outside of the anomalies, because of their considerable uncertainties we will assume here that these quantities are approximately unchanged across the relatively sharp anomaly boundaries. Therefore, the higher thermal inertia in the anomalous regions can be taken to result primarily from growth of the effective contact region between grains.

Alternative models developed for heat transport in dust layers have been used to fit experimental data for silicates and glass beads where k_{eff} depends linearly on the R_{con}/r_g (Gundlach and Blum, 2012), as opposed to the quadratic dependence in Eq. (2). It has been shown (Batchelor and O'Brien, 1977; Cooper et al., 1969) that when the thermal conductivity of the contact material is greater than the grains, $k_{cem} \gtrsim k_g$, and R_{con} is sufficiently large, the temperature of the two grains is approximately uniform in the contact region. This results in a heat flux between the grains that varies as $1/\sqrt{R_{con}^2 - r^2}$, where r is the distance from the center of the contact in Fig. 2, and implies that the effective thermal conductivity is proportional to the radius of the contact. However, if the thermal conductivity in the contact region is much lower than in the grain, either due to a rough grain boundary or a very small contact radius, then the temperature will differ on the two sides of the contact and will be approximately uniform within each grain. In this case, the temperature difference across the interface can be much larger than within a single grain and the flux through the contact is proportional to the contact area as in Eq. (2).

In order to further examine this dependence, the continuum models developed in Piqueux and Christensen (2009) for two spherical grains connected by an ideal contact volume as in Fig. 2 were used to determine the relative temperature and heat flux in the contact region. Calculations were run for $\chi = 1 \times 10^{-7}$ to 1×10^{-1}, defined by Eq. (1), and for a wide range of grain and cementation thermal conductivities (Piqueux and Christensen, 2009). Taking the thermal conductivity of the cementation and grain to be equal ($k_g = k_{cem} = k_{ice}$) and using a simple cubic configuration where $N_c = 6$, temperature and heat flux maps are shown in Fig. 3 and the derived k_{eff} is given in the caption. For $\chi \geq 1 \times 10^{-5}$ the heat flux is largest at the edges of the grain contact resulting in a linear dependence of k_{eff} on R_{con} as expected for a sufficiently large contact. However, for the smallest cementation fraction simulated, $\chi = 1 \times 10^{-7}$, the heat flux is approximately uniform across the contact area. Substituting $\chi = 1 \times 10^{-7}$ into Eq. (1) gives $R_{con}/r_g \sim 0.018$ which is of the order or larger than the estimates in Table 2 for the icy moons. This suggests that for the icy regoliths the area of the contact will control the heat flow as in Eq. (2). Simulations have not yet been carried out for smaller χ, non-spherical grains or non-ideal grain contacts.

Analytical models that use a linear dependence on R_{con}/r_g require that the porosities and grain sizes for the icy regoliths are much larger than those used here. Additionally, the relatively high k_{eff} determined from the continuum models suggest that regoliths such as those found on the Saturnian moons differ significantly from smoothly connected spherical grains. Therefore, the approximate model in Eq. (2) is used as a rough estimate for the effective contact to grain radius ratios, implying that contacts are either very small or have an average thermal conductivity much less than the grains. These results are used to determine the limiting minimum and maximum values of R_{con}/r_g used in evaluation of the radiation-induced sintering rates.

3. Electron interactions with water ice

In order to determine whether the high energy electrons are able to drive the sintering of the ice grains, we must first understand the interactions of the electrons with the water molecules in the grains and the rate at which these interactions occur in the anomalous regions. Radiation processing of grains varies by location and depth on the moon surfaces depending on the local ion and electron fluxes. Though the average electron power input per grain in the anomalous regions is small ($\sim 10^{-16}$ W) and the bulk heating effects negligible, individual electron/molecule interaction events can lead to localized 'hot-spots' in the ice (Bringa and Johnson, 2004). These interactions and subsequent excitations can induce molecular diffusion and contribute to grain sintering.

For fast charged particles (ions or electrons) incident on water ice, the dominant energy loss mechanism is through ionization of the water molecules. In a solid this is referred to as electron-hole pair production, and the average energy transferred per ionization is called the W-value. Following an ionization, recombination and dissociation occur and energy spreads from the site of the

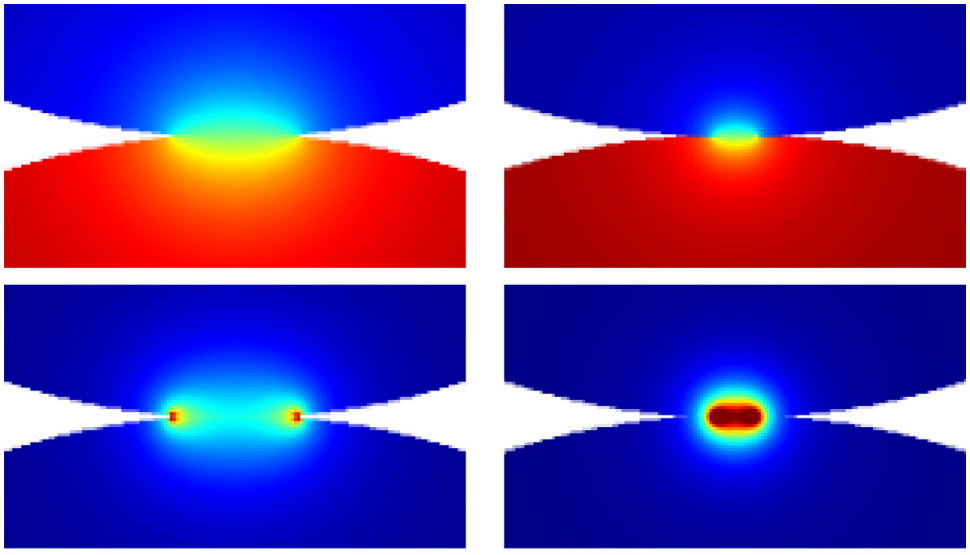

(a) $\chi = 1 \times 10^{-5}$, $R_{con} \sim 2.11\,\mu m$, $k_{eff} = 0.48\,W/(m\,K)$ (b) $\chi = 1 \times 10^{-7}$, $R_{con} \sim 0.67\,\mu m$, $k_{eff} = 0.16\,W/(m\,K)$

Fig. 3. The steady state temperature (top row) and heat flux (bottom row) distributions in the grain contact region predicted in continuum simulations of the heat transfer between water ice grains with radii of 25 μm. In column (a) the cementation volume fraction $\chi = 1 \times 10^{-5}$ and for column (b) $\chi = 1 \times 10^{-7}$ where R_{con} is related to χ using Eq. (1). The thermal conductivity of the grains and the cementation were both that of water ice, $k_{ice} = 6.5$ W/(m K), and the k_{eff} was determined for a simple cubic packing. The steady state temperature and heat flux distributions are shown by color, from blue for low values to red for high values. In the lower panels red represents high heat flux. In (a) flux is primarily through edges of contacts; in (b) flux is approximately uniform across contact area. (For interpretation of the references to color in this figure legend, the reader is referred to the web version of this article.)

initial interaction, driving molecular motion. However, the energy released directly into molecular motion is only a fraction of the initial deposited energy. The remainder is lost through vibrational excitations, heat conduction, and small momentum transfers below the defect formation activation energy (Johnson, 1990). Taking $W \sim 27$ eV for water (Vassiliev, 2012), the deposited energy per ionization available to produce molecular motion and defect formation in the bulk or desorption of molecules from the grain surface is estimated to be $\Delta E \sim 5$ eV.

In general, when the energy transferred to a molecule is greater than the cohesive energy of the solid the molecule becomes mobilized and subsequently loses energy in a cascade of molecule/molecule collisions, here called a mini-cascade, until it returns to thermal equilibrium with the solid, typically in <10 ps. In a uniform molecular material such as water ice, the total number of secondary recoils with an energy between E and $E + dE$ produced by an excited molecule of initial energy ΔE can be approximated from transport equations using

$$dN \sim \beta \frac{\Delta E}{E^2} dE \tag{3}$$

where $\beta \sim 6/\pi^2$ in Sigmund (1969) and 0.8 in Myers (1980). These results are roughly consistent with Molecular Dynamics (MD) simulations and have been used to describe electronic sputtering of ices and silicates (Bringa and Johnson, 2004; Johnson and Liu, 1996). Based on Eq. (3), the average number of molecules, N, which overcome a given activation energy, E_a, due to energy released during the cascade is roughly

$$N \sim \frac{\beta \Delta E}{E_a} \tag{4}$$

which is consistent with the well known Kinchin-Pease estimate of defect (vacancy/interstitial pair) production in the bulk where $E_a = 2U_{bulk}$. The bulk cohesive energy of crystalline water ice is $U_{bulk} \sim 0.75$ eV (Watkins et al., 2011), although it is lower in ices formed by low temperature vapor deposition.

The weighted average distance from an ionization event, λ, at which molecules can still be sufficiently energetic to overcome E_a can either be estimated analytically or derived from MD simulations (Johnson and Liu, 1996). A rough approximation of this length is given by

$$\lambda \approx \frac{\ell_0}{4} N \tag{5}$$

where $\ell_0 \sim 0.3$ nm is the approximate lattice spacing for water ice. It is important to note that the cohesive energy of water ice is lower at the surface than in the bulk so that vacancies form more readily. Watkins et al. (2011) found vacancy formation energies of $0.2 - 0.5$ eV per molecule in the uppermost complete monolayer. These decreased further as additional vacancies were added to the surface with vacancy formation energies as low as ~ 0.1 eV found in some vacancy complexes. A range of activation energies for several diffusion processes is given in Table 4.

The PENELOPE (Penetration and ENErgy LOss of Positrons and Electrons) Monte-Carlo program (Salvat and Sempau, 2011) was used to simulate the energy deposited in ionizations and excitations by MeV electrons incident on a semi-infinite amorphous water target. PENELOPE calculates the electron energy loss due to elastic and inelastic collisions, inner shell ionization, and Bremmstrahlung, although the latter two are orders of magnitude less efficient in the relevant energy ranges (< 10 MeV). The simulations were run by sampling 1×10^8 electrons from the measured electron energy distributions in the vicinity of the Saturnian moons, given in Fig. 4a. Results are given for both normal incidence and averaged over a cosine distribution of electron incidence angles in Fig. 4b. The low energy cut off of the electron energy distribution was taken to be $\mathcal{E}_{cr}$, given for each body in Table 1, and the upper cut off where the electron intensity falls to negligible levels (≤ 10 MeV). The mean energy of the electrons impacting the moon surfaces decreases with distance from Saturn meaning that the regolith depths affected by the electrons also decrease as seen in Fig. 4b.

Taking the incident electron flux, Φ_{elec}, from Table 2 (Paranicas et al., 2012), the ionization rate of molecules in

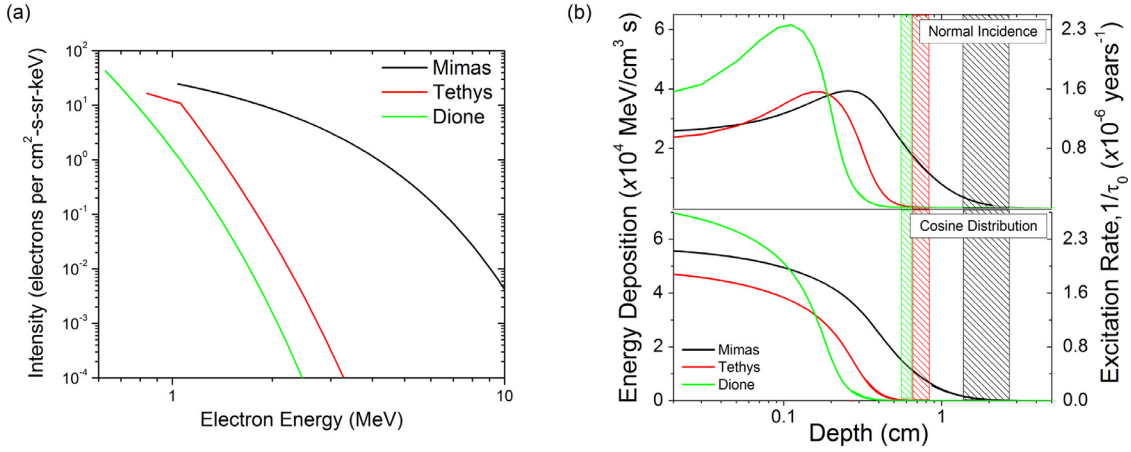

Fig. 4. (a) Energy spectra of electrons in the vicinity of the icy moons based on LEMMS measurements taken from Paranicas et al. (2012) where the lower limit is taken as $\mathcal{E}_{cr}$ given in Table 1. (b) The average energy flux deposited per unit length calculated with the PENELOPE program using the electron probability distributions shown in (a). The upper frame gives the deposition profile for normally incident electrons and the lower panel gives results for electrons averaged over a cosine distribution of incidence angles. The hashed boxes show the measured thermal skin depth and are consistent with the penetration depth of the electrons for a 50% porous regolith.

the solid grains is

$$\frac{1}{\tau_0} = \left(\frac{dE}{dz}\right)\frac{\Phi_{elec}}{n_0 W} \tag{6}$$

where $n_0 \sim \ell_0^{-3}$ is the molecular number density and dE/dz is the average energy deposited per electron per unit depth into the regolith as calculated by PENELOPE. The left hand axis of Fig. 4b shows the average energy flux deposited per unit length as a function of depth below the surface of a water ice regolith with $\phi = 0.5$, and the right hand axis gives the molecular ionization rate calculated from Eq. (6). The excitation rate is the frequency at which a single molecule will be ionized by the incident electron flux. The hashed boxes represent the approximate thermal skin depth given in Table 1. In the following, the excitation rates and the diffusion length of mobilized molecules are used to estimate the radiation-induced sintering timescales.

4. Grain modification processes on icy satellites

In this section, we give rough estimates for the grain sintering timescale due to radiation interactions with low temperature porous ices and regolith resurfacing timescales due to dust grain infall to the moons. The specific nature of the grain sintering mechanisms depends on the grain and contact geometries and molecular bonding arrangement in the contact region. The very low thermal conductivities outside the anomalous regions are difficult to explain unless the grains are characterized by large surface roughness and high porosities. Radiation-induced diffusion tends to smooth rough grains, thus minimizing the surface energy, and sintering occurs when an excited molecule moves into a defect site in the grain contact region.

For simplicity, we consider a sintering timescale to be the time needed to increase the grain contact radius R_{con} from the minimum to the maximum values implied by the thermal inertia measurements in Table 1, without interruption due to regolith renewal processes. In the following calculations we use $1/\tau_0$ estimated from the bottom panel of Fig. 4b. Taking the volume surrounding the contact in which an electron/molecule interaction can occur and contribute to sintering to be V_{int} and using Eq. (4), the average number of molecules mobilized per event, N, per unit time in V_{int} is

$$\frac{d\mathcal{N}}{dt} = \frac{N n_0}{\tau_0} V_{int}. \tag{7}$$

However, not every mobilized molecule in V_{int} will contribute to sintering, and thus we take the probability of a molecule diffusing into a lower energy site in the contact region, ε, times the volume of a molecule, $\sim 1/n_0$, as the average increase of the contact volume per excited molecule in the contact region. The resulting sintering rate estimate is then given by

$$\frac{dV_{con}}{dt} \sim V_{int}\frac{\varepsilon N}{\tau_0} = \frac{V_{int}}{\tau_{sint}} \tag{8}$$

where the quantity εN determines the number of molecules diffusing and depends on the local ice structure (e.g., defect structure and vancacy concentration) where the ionization event takes place. That is, irregular surfaces or the presence of poorly bound molecules means that ε and N are larger than, for instance, in a highly crystalline contact region. If we assume that V_{int} is of the order V_{con} and that εN is independent of V_{con}, then the sintering timescale $\tau_{sint} \sim \tau_0/\varepsilon N$.

4.1. Experimental estimate of sintering timescale

In recent experimental work, a large reduction in the porosity of vapor deposited laboratory ices was produced by energetic ions (Raut et al., 2008; Dartois et al., 2015; 2015). Although the laboratory ices were thin ($< 1\,\mu m$) with an initial porosity of only 26%, they can be considered crude proxies for a contact region with local roughness such as that shown in the Fig. 2 inset. As is the case for electrons, the incident ions (~100 keV to MeV) deposited energy predominantly through ionizations which in turn drove molecular diffusion. Fitting the porosity measurements as a function of energy deposited in the ice with a decreasing exponential and ignoring any low energy thresholds (Dartois et al., 2015; 2015) results in a characteristic energy of $E_c \sim 1.3$ eV. This accounts for both the fraction of deposited energy converted into molecular motion and for the efficiency of the annealing process that leads to compaction of the porous sample. Equating the sintering timescale given above with the compaction timescale then a first order estimate for the sintering timescale can be written $\tau_{sint*} \sim \tau_0(E_c/W)$, and it is seen that $\varepsilon N \lesssim 20$, implying that each ionization creates a large number of mobilized molecules which subsequently move into more favorable binding sites. For comparison, using $\Delta E \sim 5$ eV and $E_a \sim 0.5$ eV, which is a conservative value for surface diffusion activation energy of crystalline laboratory ices (Nie et al., 2009), then Eq. (4) gives $N \sim 6-8$. Although these are similar orders of magnitude, the compaction measurements were made on ices deposited from the vapor at very low temperatures. Therefore, the

Table 3
Comparison of molecular excitation timescale (τ_0), sintering timescale derived from compaction experiments (τ_{sint^*}) and resurfacing timescales (τ_{gar} and τ_{gro}) for the icy Saturnian moons. The length scales represent effective regolith depths. Appendix B reproduces the method used to estimate τ_{gar} due to meteorite gardening, which is approximately uniform across the bodies, and τ_{gro} due to E-ring grain deposition, which fall preferentially on the trailing hemisphere of Mimas and the leading hemispheres of Tethys and Dione. The sintering* timescale is approximated from experimental results measuring ion-induced compaction of porous ices and predicts shorter timescales than for gardening or deposition.

Timescale [Myr]	Molecular excitation τ_0 (1 mm)	Sintering* τ_{sint^*} (expt.)	Meteorite gardening τ_{gar} (1 cm)	E-ring growth τ_{gro} (1 cm)
Mimas	0.5	0.02	0.9	–
Tethys	0.7	0.03	3.0	0.1
Dione	0.7	0.03	7.5	0.5

molecular structure is highly disordered, consistent with the larger value of εN above.

Compaction not only reduces the porosity of the solid but, of interest here, it would improve the thermal contact between individual ice particles. The large value estimated for εN suggests that the ΔE contributing to the compaction could be a larger fraction of the deposited energy W than that estimated from experiments on ion sputtering of ice (Johnson, 1990). Although the energy deposition densities for the ions in the compaction experiments were typically higher on average than the MeV electrons considered here, the maximum energy deposition in Fig. 4b is comparable to the lowest experimental values. Therefore, the compaction results represent a rough lower bound for the sintering timescale.

4.2. Regolith growth timescale

Gardening due to impacts from interplanetary dust particles (IDPs) and meteorites, as well as the deposition of circumplanetary material such as E-ring grains ($\lesssim$ μm), compete with sintering in determining the steady state regolith surface properties. In order for the observed anomalies to be stable on the icy satellites, the sintering timescale should be less than or comparable to the regolith renewal timescales due to impacts. At Mimas, the E-ring grains deposit preferentially on the trailing side and are neglected in estimates of the resurfacing timescale of the leading hemisphere where the thermal anomaly is located. On Tethys and Dione, E-ring grains deposit preferentially on the leading side, coating the anomalous regions (Hamilton and Burns, 1994). The IDPs are assumed to bombard the surface isotropically and due to gravitational focusing by Saturn the fluxes at Mimas are the largest. Table B.6 gives estimates for E-ring deposition rates derived from Voyager measurements (Spahn et al., 2006a) and the IDP flux at Saturn (Poppe, 2016).

The IDP grains impact the moon surfaces at large velocity ($\sim$ 20 km/s), produce melts and scatter ejecta on the surface. However, the E-ring grains have a smaller relative velocity (5−7 km/s) with respect to the moons (Spahn et al., 2006a) and cause less mixing while depositing additional ice onto the surface. Much of the ejecta produced by E-ring grains falls back to the surface as fresh icy microstructures, thus producing the high observed geometric albedos (Verbiscer et al., 2007). Although the hemispherical dependence of surface processing due to impacts at Tethys and Dione will differ from that at Mimas, we here assume that the electrons sinter the grains in a similar manner for all bodies. The regolith formation timescales due to E-ring grains and IDPs are given in Table 3. These estimates are very rough and improved modeling of E-ring grain distributions, spatially dependent deposition rates, and impact effects are needed to determine how grain deposition modifies the surfaces of icy moons. However, the ion compaction experiments suggest that the incident MeV electron flux is able to produce the requisite sintering faster than the expected regolith renewal rate so that stable thermal anomalies can form. In order to further test these conclusions, we now consider sintering processes using standard models for spherical grains where diffusion is driven by electron radiation.

Table 4
Thermal diffusion coefficients and activation energies where $D = D_o exp(-E_a/kT)$. The range of activation energies for each diffusion process represents uncertainty in the experimental measurements. The maximum and minimum activation energies can be thought to represent smooth and rough grains, respectively.

Diffusion Mechanism	D_0 [cm^2/s]	E_a [eV]
Bulk, D_{bulk}[a]	$\sim 10^{-11} - 10^{8}$	0.6 – 0.75
Surface, D_{surf}[b]	$1.4 \times 10^{-4} - 6.1 \times 10^{-3}$	0.1 – 0.5
Grain Boundary, D_{gb}[c]	8.4	0.51
Vacancy, D_v[d]	1×10^{-3}	0.62

[a] Livingston et al. (1998); Nasello et al. (2007)
[b] Kouchi et al. (1994); Nasello et al. (2007); Nie et al. (2009)
[c] Goldsby and Kohlstedt (2001)
[d] Hobbs (1974)

5. Sintering of spherical grains

The molecular excitation rates derived from electron fluxes measured in the vicinity of the icy moons of Saturn and activation energies measured in ice irradiation experiments suggest that high energy electron sintering can explain the observed thermal anomalies. However, sintering estimates given in Table 3 do not take into account the grain size, shape, or residence time on the surface. Furthermore, the relevant diffusion paths which lead to accumulation of molecules in the contact region between grains are ignored. Here we describe a means of calculating effective radiation-induced diffusion coefficients and the corresponding sintering rates for monodisperse spherical grains of varying size. The model calculates the grain contact radius as a function of radiation fluence and allows improved estimates for the sintering timescales.

Electron ionization events in the water ice regolith can desorb molecules from grain surfaces and induce bulk, surface, and grain boundary diffusion, leading to a growth in the contact volume as shown schematically in Fig. 5. Descriptions of the sintering rate dependence on geometric and thermodynamic properties were originally developed in powder metallurgy (Kuczynski, 1972; Swinkels and Ashby, 1981) and depend on the size of the grains, temperature, external pressure, and vapor pressure in the void space. The model described in Appendix C assumes idealized spherical grains under thermal equilibrium. However, regolith grains are likely not spherical, the contacts not ideal, and the production of molecular motion following ionization events is inherently non-equilibrium. Additionally, at the low temperatures measured on these icy satellites, the thermal diffusion times are much greater than $\sim$ 1 Myr so that the defect densities are not at thermal

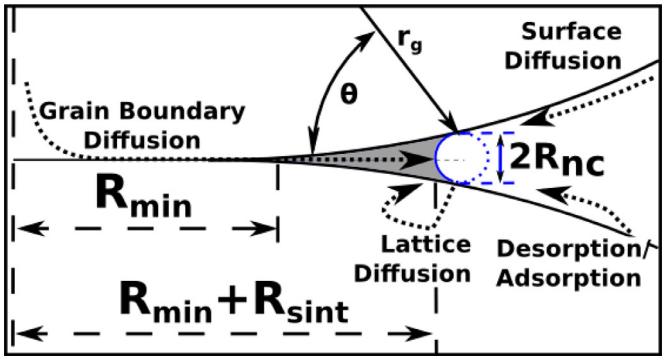

Fig. 5. Diffusion paths and approximate contact shape for spherical grains where R_{min} is the contact radius of freshly deposited grains and increases due to sintering. The inverted curvature where the grains come into contact provides an increase in the number of bonds available to a surface molecules and therefore represents a surface energy minimum. Assuming that $R_{con} = R_{min} + R_{sint} \ll r_g$, we see $\theta \sim \pi/2$ and $R_{nc} \sim {R_{con}}^2/2r_g$.

equilibrium as assumed in the sintering models. Therefore, the results described below provide rough upper limits for the sintering timescales.

5.1. Sputtering and redeposition

Sintering of ice grains is well studied at terrestrial and cometary temperatures where the dominant mechanism is typically found to be vapor transport of molecules (Blackford, 2007; Sirono, 2011). For thermally driven, gas phase sintering, the rate of change in the contact volume connecting equal sized grains can be written

$$\frac{dV_{con}}{dt} = 2\pi R_{con} R_{nc} \theta \frac{\Phi_v}{n_0} \xi_{vapor} \tag{9}$$

where R_{nc} and θ are indicated in Fig. 5, Φ_v is the net vapor flux at the surface, and ξ_{vapor} accounts for surface energy and grain curvatures as descibed in Appendix C. However, at 80K thermal vapor pressure is very low and the primary source of gas phase molecules in the anomalous regions is likely electron-induced desorption of molecules from grain surfaces. For a flat surface, the molecular desportion flux can be estimated from

$$\Phi_0 \sim \frac{\lambda n_0}{\tau_0} \tag{10}$$

where n_0 is the number density of the ice grains and τ_0 can be determined from Fig. 4. The linear dependence of λ on the energy deposition has not been well studied, but is clearly seen in laboratory measurements of UV photon and energetic electron irradiation of ice at low temperatures (Westley et al., 1995). Assuming that the mini-cascade is approximately spherical, the sputter flux for a curved surface is given by (Urbassek et al., 2015; Wei et al., 2009)

$$\Phi_{sput} \sim \Phi_0[1 + \lambda(K_{11} + K_{22})/2] \tag{11}$$

where λ is estimated using Eq. (5) and K_{11} and K_{22} are the principle surface curvatures measured along the axes perpendicular to the surface normal. For a flat surface, $K_{11} = K_{22} = 0$, and for a sphere of radius R, $K_{11} = K_{22} = 1/R$.

At temperatures below 100 K the sticking probability of water molecules is ~ 1 (Gibson et al., 2011) and, accounting for electron-induced sputtering and thermal vapor pressure, the mean free path of the ejected molecules is much larger than the pore diameter. If there are no gas phase collisions and no scattering from grain surfaces, then only molecules with a direct line-of-site path to the grain contact will contribute to contact growth. Therefore, one might assume the local geometry of the regolith would be important. However, assuming a uniform grain size distribution, Sirono (2011) found little difference between the growth rates determined using a molecular mean free path much larger or much smaller than the grain radius. Noting that, on average, gas phase molecules in a spherical grain regolith originate on surfaces with curvature $1/r_g$, the net sputter flux at a point in the contact region is the difference in the deposition and ejection rates and is given by

$$\Phi_{net} = \Phi_0 \frac{\lambda}{2}\left(\frac{2}{r_g} - \frac{1}{R_{con}} + \frac{1}{R_{nc}}\right) = \Phi_0 \xi_{sput}. \tag{12}$$

For the case of $r_g \gg R_{con}$, the neck radius, $R_{nc} \sim {R_{con}}^2/2r_g$, dominates the curvature term and, substituting Eq. 10 and Eq. 12 into Eq. C-3, we can write $\tau_{sint} \sim ({R_{con}}^3\tau_0)/(\pi\lambda^2 r_g)$. Taking approximate values of $R_{con}/r_g \sim 0.01$ and $\tau_0 \sim 0.5$ Myr and using $E_a \sim 0.5\,eV$ in Eq. (5), then $\tau_{sint} \sim 300$ Myr and 30 Myr for 25 μm and 5 μm grains, respectively. This is much longer than the regolith formation timescales, suggesting that sputtering and redeposition rates are small so that the diffusion processes discussed below dominate grain sintering for the contact size ranges given in Table 2.

5.2. Radiation-induced diffusion

In general, when a molecule in the water ice grains is excited by charged particle radiation, several regimes of induced diffusion can be identified (Myers, 1980). The first, often referred to as the mixing phase, is driven by the mini-cascade produced when an excited molecule releases energy to the surroundings through a series of collisions. Mixing in this context differs from impact produced mixing in that it affects the solid on the order of only nm as opposed to μm in the case of grain impacts. Following the mini-cascade, the heat diffuses away and can still, in principle, activate a sintering event. However, this thermal pulse has not been well modeled and more studies are needed to determine to what extent excitation energies below the diffusion activation energies can contribute to grain sintering in an icy regolith. Finally, enhanced bulk diffusion occurs due to increased concentrations of vacancies and interstitials resulting from the electron radiation. As most previous studies of radiation-induced diffusion in solids have focused on ion bombardment of metals and semi-conductors, care must be exercised in adapting models to electron irradiation of a dielectric ice with non-equilibrium defect density.

During the mini-cascade, on average N molecules, estimated using Eq. (4), will become energetic enough to overcome the diffusion activation energy E_a. Experimentally measured activation energies for each of the diffusion process depicted in Fig. 5 are given in Table 4 where the range of values represents the large experimental uncertainty. The effective diffusion coefficient associated with the mini-cascades, D_{mc}, can be written

$$D_{mc} = \frac{N{\ell_{eff}}^2}{J\tau_0} \tag{13}$$

where ℓ_{eff} is the mean diffusion length of molecules excited in the minicascade and $J = 6$ or 4 for bulk and grain boundary diffusion or surface diffusion, respectively, and represents the degrees of freedom in which a molecule can diffuse.

The mean diffusion length can be estimated using the often applied thermal spike models (Kaoumi et al., 2008). These models assume energy deposited in ionization events is initially localized in a small number of nearby molecules and spreads uniformly outward. The heat distribution is integrated over time assuming constant thermal conductivity and heat capacity of the material to determine the effective diffusion coefficient, from which ℓ_{eff} can be determined. However, experimentally determined values for both

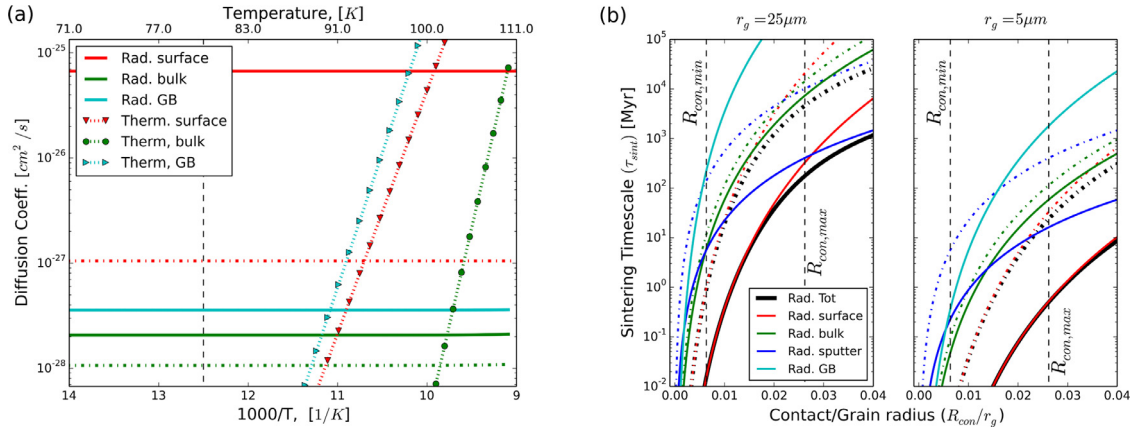

Fig. 6. (a) Radiation-induced diffusion coefficients at Mimas calculated from Eq. (13) and compared with the bulk (Livingston et al., 1998), grain boundary (Goldsby and Kohlstedt, 2001), and surface (Kouchi et al., 1994) thermal diffusion coefficients. The dashed vertical line indicates 80 K. (b) Sintering timescales $\tau_{sint} \sim V_{con}/(dV_{con}/dt)$ at 80 K calculated using the sintering model of Swinkels and Ashby (1981) and effective radiation-induced diffusion coefficients determined for the energy deposition rates at Mimas. Here, the vertical dashed lines represent the limits of R_{con}/r_g for Mimas taken from Table 2 assuming $\phi = 0.5$ and $k_g = 6.5$ W/m/K. For both images, the solid lines are for the minimum activation energies given in Table 4 and can be thought to represent a 'rough' grain where radiation induced diffusion is efficient, while the dashed-dot lines were calculated using the maximum energies and represent smooth, crystalline grains.

E_a and the jump frequency of molecules are needed. Due to difficulties in measuring molcular diffusion at low temperatures and differing growth conditions there is a large spread in these parameters as seen in Table 4. Estimating the jump frequency using the entropy change due to vacancy formation and migration and the Debye frequency of vibration (Hobbs, 1974; Shewmon, 1963) and taking $E_a \sim 0.5$, thermal spike models give a range $\ell_{eff} \sim 1 - 50\,\ell_0$. Noting that the lower estimates of ℓ_{eff} obtained from thermal spike models are similar to the approximate cascade size obtained from Eq. (5), we use the latter as a conservative estimate of mean effective diffusion length.

Enhanced bulk diffusion results from defect concentrations that are greater than expected for a material in thermodynamic equilibrium. The vacancy/interstitial pairs created during a mini-cascade event will diffuse through the solid until they either (a) recombine through thermal diffusion or (b) annihilate at a fixed sink such as a grain surface (Myers, 1980). The defect pair creation rates can be roughly estimated from Eq. (4). The model of enhanced bulk diffusion presented by Myers (1980) assumes that any spatial variations are small and that the vacancy and interstitial concentrations are in steady state (balanced annihilation and creation rates). Based on the vacancy diffusion rate in Table 4, enhanced bulk diffusion is here assumed to be negligible at 80 K.

5.3. Spherical grain sintering timescales

The radiation-induced surface, bulk, and grain boundary diffusion coefficients determined using Eq. (13) and assuming the radiation conditions on Mimas are plotted in Fig. 6a. For temperatures of 80 K, radiation induced diffusion dominates thermal diffusion, although thermal grain boundary and surface diffusion become comparable at temperatures approaching 100 K. Details of the sintering process are given in Appendix C, and the sintering rates are estimated by replacing the thermal diffusion coefficients in Eqs. C-4a–c with the radiation-induced diffusion coefficients. The sintering rate for spherical grains depends sensitively on the relative sizes of the grain and contact regions. Assuming $R_{con} \ll r_g$, it can be shown that τ_{sint} varies as $R_{con}{}^5/r_g^2$ for the bulk and $R_{con}{}^7/r_g^3$ for the surface sintering mechanisms. The sintering timescales at Mimas, $\tau_{sint} \sim V_{con}/(dV_{con}/dt)$, are shown in Fig. 6b. Surface diffusion tends to dominate in the size ranges of interest and smaller grain sizes have shorter sintering timescales due to the proportionately larger curvatures and an increased probability of an excitation occurring close to a grain contact. Assuming constant sintering rates in a regolith of uniform 25 μm grains, an activation energy of $E_a \sim 0.5$ eV, and $R_{con}/r_g \sim 0.01$ gives $\tau_{sint} \sim 50$ Myr for bulk and ~ 10 Myr for surface diffusion sintering timescales, respectively. For 5 μm grains the surface diffusion sintering mechanism dominates with $\tau_{sint} \sim 0.1$ Myr.

The estimated contact to grain radius ratios inside and outside the anomalous region of Mimas, taken from Table 2, are indicated in Fig. 6b, and the timescale for sintering is determined by numerically integrating the total sintering rate over this interval. This is done for each body assuming a constant average temperature of 80 K, and the resulting timescales are given in Table 5. The range of sintering timescales is determined from the uncertainty in the measured thermal inertia, and the *max* and *min* values correspond, respectively, to the upper and lower limits of the diffusion activation energies in Table 4.

Assuming that the gardening and E-ring grain deposition rates in Table 3 dominate the regolith resurfacing processes and that the model for k_{eff} in Eq. (2) gives reasonable estimates for the contact radii, the results in Table 5 indicate that only certain regolith geometries give reasonable sintering timescales. At Mimas and Tethys, this model suggests that either regolith growth/mixing timescales are longer than those in Table 3 or the regolith is relatively compact and composed of small, rough grains. That is, unless $r_g \lesssim 5$ μm, $\phi \lesssim 0.65$, and the E_a for surface diffusion is near the lower limits established in experiments, the calculated sintering timescales for spherical grains are greater than the estimated regolith renewal timescales. However, these latter estimates also have considerable uncertainties. The thermal anomalies on Dione and Tethys are much smaller than those on Mimas. This is due to both the smaller penetration depth of the electrons and the obscuration of the effect by the more rapid regolith mixing consistent with the smaller resurfacing times in Table 3.

6. Conclusion

Thermal anomalies on the icy Saturnian moons of Mimas, Tethys and Dione have been spatially correlated with high energy electrons which preferentially impact the leading hemispheres of these bodies. The thermal inertia increase in the irradiated regions has been suggested to be due to an increase in the effective size of the contacts connecting adjacent grains. A simple model for the thermal conductivity of the regolith indicates that the effective contact radii are much smaller than the grain radii. This is consistent with a poor thermal contact between grains, possibly due

Table 5
Electron-induced sintering times in Myr for the icy Saturnian moons. The radiation enhanced sintering model is sensitive to R_{con}/r_g and the values given in Table 2 were used to determine the initial and final sintering rates. The *min* values correspond to the smallest activation energies given in Table 4 and can be thought represent a 'rough' grain with a high defect density , while the *max* values approximate smooth, crystalline grains.

τ_{sint} [*Myr*]	$r_g = 25\,\mu m$ $\phi = 0.5$ $k_g = 6.5$ W/m/K	$r_g = 5\,\mu m$ $\phi = 0.5$ $k_g = 6.5$ W/m/K	$r_g = 5\,\mu m$ $\phi = 0.65$ $k_g = 6.5$ W/m/K	$r_g = 5\,\mu m$ $\phi = 0.5$ $k_g = 0.5$ W/m/K
Mimas				
max	800 – 5000	3 – 30	30 – 300	> 1000
min	30 – 200	0.06 – 0.7	0.7 – 7	100 – 500
Tethys				
max	3 – 9	0.01 – 0.02	0.07 – 0.2	20 – 60
min	0.06 – 0.2	$\sim 10^{-4}$	$\sim 10^{-3}$	0.5 – 1
Dione				
max	0.007 – 0.1	$\sim 10^{-4}$	$\sim 10^{-3}$	0.06 – 1
min	$\sim 10^{-3}$	$< 10^{-6}$	$\sim 10^{-5}$	0.001 – 0.02

to highly irregular grain shapes. We note that the competing regolith formation processes on the these satellites are not well constrained and there are no available thermal models for a regolith composed of irregular grains. Furthermore, spectral reflectance observations at different wavelengths give a range of grain radii on the various icy satellites from sub-micron (Nelson et al., 2015; Scipioni et al., 2015) to $\sim$ 25 μm (Filacchione et al., 2010; Hendrix et al., 2012), and the varying reflectance with wavelength suggests changing regolith structure with depth (Schenk et al., 2011). Therefore, in this paper we provide rough bounds on the timescales for the radiation-induced alteration of the thermal properties of the regolith.

We show that the proposed radiation-induced sintering mechanism can produce the stable thermal anomalies consistent with grain impact resurfacing estimates. Estimates for the sintering times based on experimental results indicate that, under reasonable approximations for grain structure and molecular excitation rates, radiation-induced sintering is faster than the approximate regolith renewal rate. The smaller thermal inertia differences measured on Tethys and Dione imply that E-ring grain infall limits the strength of the anomalies on these bodies, while IDP gardening limits the anomaly strength at Mimas. This is also consistent with the suggestion that the differences in the reflectance spectra inside and outside the anomalous regions observed by Voyager and Cassini are due to the electron radiation. A standard spherical grain sintering model which depends on the regolith porosity, grain size, and grain thermal conductivity was also used to estimate radiation-induced diffusion and sintering rates. This model assumes idealized contacts between grains and defect densities that are at thermal equilibrium, and therefore gives only an approximate upper limit to the sintering timescale. The spherical grain models suggest that the regoliths have a porosity $\lesssim$ 65% and grain sizes of $\lesssim$ 5 μm.

The radiation-induced sintering rates depend sensitively on how electron-deposited energy spreads in the grains and near the contact regions. Further work is needed for a variety of ice samples in order to better understand the microphysics of the sintering process. Due to the difficulty of such experiments, MD simulations can be used to constrain the number of mobilized molecules per ionization event, the extent of the collision cascade, and the overall efficiency of the resulting radiation-induced sintering processes for non-spherical water ice grains. Continuum simulations can also be used to better describe the effective thermal conductivity between irregular grains with irregular contact regions. Such simulations are in progress and will be used to further improve the sintering calculations presented here in order to better understand weathering phenomena in ices and help constrain regolith properties.

Acknowledgments

The authors would like to thank C. Howett and A. Verbiscer for helpful conversations about the remote observations of the anomalous regions and useful comments on the manuscript. Finally, we would like to thank referee C. Paranicas for helpful comments on the manuscript and explanations of the electron counter-rotational effect. M. J. Schaible and R. E. Johnson would like to acknowledge support by SwRI through the JPL Cassini mission and NASA's Planetary Geology and Geophysics program. The work of S. Piqueux was carried out at the Jet Propulsion Laboratory, California Institute of Technology, under a contract with NASA.

Appendix A. Hertzian contact radius

Deformation of curved, elastic surfaces in contact was first studied by Heinrich Hertz in 1882, and so-called 'Hertzian analysis' can be used to determine the intergranular contact area for dissimilar bodies. The contact radius between two spheres depends on the material properties and is related to an applied load F by

$$R_{Hertz} = \left[\frac{3}{4}\frac{1-\nu(T)^2}{Y(T)} r_g F\right]^{1/3} \tag{A-1}$$

where $\nu(T)$ and $Y(T)$ are the temperature dependent Poisson's ratio and Young's modulus of the material, respectively. The applied load determines how strongly adjacent particles are bonded and the weight of the grains can be used to determine the force as a function of depth. However, for grains with little force pressing them together, such as those at the surface of a loose regolith, van der Waals bonding provides orders of magnitude greater adhesion than gravitational forces. Taking the adhesive force as the tensile force needed to separate the spheres, this can be estimated by the so-called JKR theory as (Johnson et al., 1971)

$$F_{JKR} = 3\pi\gamma_s r_g \tag{A-2}$$

where γ_s is the specific surface energy of the material at the solid/solid interface. The Hertzian contact radius is sometimes used in thermal conductivity expressions for non-cemented grains to describe the effective grain contact radius.

Appendix B. Meteorite gardening

Resurfacing on the inner saturnian moons is driven by E-ring grains and interplanetary dust pasticles (IDP). The IDP impacts eject and distribute the surface material, and the average yield per impact, Y =mass of ejecta/mass of impactor, depends on the mass and relative velocity of the impactor (Spahn et al., 2006a). The IDP mass flux and velocity near Saturn are taken to be $\sigma_\infty \sim 1 \times 10^{-18}$

g/cm^2/s (Poppe, 2016) and $v_\infty \sim 9.5$ km/s (Spahn et al., 2006a), respectively. The E-ring impact velocity is lower than for IDPs with lower ejecta and less mixing so that we assume the grains primarily coat the surface.

To calculate the regolith gardening rate due to IDP grains, we determine the ejecta rate of surface material due to impacting IDPs (Cuzzi and Estrada, 1998)

$$\sigma_{IDP} = f_g \sigma_\infty Y \tag{B-1}$$

where f_g is the gravitational focussing factor and the yield Y is taken from Spahn et al., 2006b. The depth h to which the regolith grows in time t can be written

$$h_{IDP}(t) = \frac{\sigma_{IDP}}{\rho_{reg}} t (1 + t/t_0)^{-0.55} \tag{B-2}$$

where h is in μm and the mixing timescale is $t_0 \sim 1.7 \times 10^5$ years (Cooper et al., 2001). The rate at which E-ring grains cover the surface, given as a mass flux σ_{E-ring}, can be used to directly determine the total rate at which the regolith is coated. The growth rate of the regolith is determined by dividing the flux by the density of the regolith, and the timescale for the regolith to grow to a depth h can be written

$$\tau_{E-ring}(h) = \frac{h \rho_{reg}}{\sigma_{E-ring}}. \tag{B-3}$$

The IDP and E-ring grain fluxes onto the surfaces and IDP yields are shown in Table B.6, and the timescales for the individual processes to produce a regolith of 1 cm depth are given in Table 3.

Appendix C. Sintering rate equations

When grains come into contact, free energy variations and concentration gradients cause molecular and atomic diffusion, and molecules tend to accumulate in the contact region between grains and sinter grains together. The sintering of spherical grains under various conditions of temperature and pressure can be calculated using equations given in Swinkels and Ashby (1981), and the mechanisms that are imporant for radiation sintering of ice grains in the upper ~ mm of the regolith are shown in Fig. 5. The equation for vapor phase sintering is

$$\left(\frac{dV_{con}}{dt}\right)_{vapor} = 2\pi R_{con} R_{nc} \theta \frac{\Phi_v}{n_0} \xi_{vapor} \tag{C-1}$$

where ξ is the 'sintering efficiency' and

$$\Phi_v = \frac{P_v(T)}{(2\pi m k T)^{1/2}}$$

is the net vapor flux at the surface due to thermal desorption and absorption. Here, $P_v(T)$ is the temperature dependent vapor pressure, m is the mass of the gas species (=18 amu for water), k is the Boltzmann constant, n_0 is the number density of molecules in the grain, and T the average temperature. Sintering is driven by the minimization of the total surface energy due to the difference in curvatures between the grain and the neck regions and

$$\xi_{vapor} = \frac{\gamma_s}{n_0 k T} \left(\frac{2}{r_g} - \frac{1}{R_{con}} - \frac{1}{R_{nc}}\right). \tag{C-2}$$

where, assuming that the grain interpenetration depth is zero, $R_{nc} = {R_{con}}^2/[2(r_g - R_{con})]$ is the curvature of a smoothly connected neck as shown in Fig. 5 and $\gamma_s \sim 300$ erg/cm^2 or 0.4 eV per molecule is the specific surface energy of the water ice/vapor interface (Henry, 2003). The rate of change in contact radius is the volume sintering rate divided by the area of the neck region, $\sim 2\pi R_{con} R_{nc} \theta$. Assuming $r_g \gg R_{con} \gg R_{nc}$ this gives

$$\left(\frac{dR_{con}}{dt}\right)_{vapor} = \frac{2\Phi_v}{n_0^2} \frac{\gamma_s}{kT} \frac{1}{R_{nc}}. \tag{C-3}$$

This implies that when the contact radius is much smaller than the grain radius, the vapor phase sintering rate is dominated by the curvature of the neck region and will decrease as the contact region grows larger.

The bulk, surface, and grain boundary sintering mechanisms depend on the diffusion rate of molecules, and are given by Swinkels and Ashby (1981).

$$\text{Bulk diffusion: } \left(\frac{dV_{con}}{dt}\right)_{bulk} = 3\pi R_{con} D_{bulk} \xi_{bulk} \tag{C-4a}$$

$$\text{Surface diffusion: } \left(\frac{dV_{con}}{dt}\right)_{surf} = 3\pi R_{con} D_{surf} \xi_{surf} \tag{C-4b}$$

$$\text{Grain boundary: } \left(\frac{dV_{con}}{dt}\right)_{GB} = 16\pi \frac{D_{gb}}{R_{con}} \xi_{GB} \tag{C-4c}$$

For the surface and bulk sintering mechanisms, as in vapor phase sintering, material is redistributed from the grain surfaces into the contact region resulting in no net change in regolith density or porosity. The sintering efficiency for bulk sintering is the same as for vapor phase, $\xi_{bulk} = \xi_{vapor}$, while the efficiency for surface diffusion sintering is given by

$$\xi_{surf} = \frac{\gamma_s}{n_0 k T} \frac{\delta_s}{d_s} \left(\frac{2}{r_g} - K_s\right) \tag{C-5}$$

where δ_s is the approximate surface thickness and d_s, and K_s are described in Swinkels and Ashby (1981). Noting that for $r_g \gg R_{con}$ the neck curvature simplifies to $R_{nc} \sim {R_{con}}^2/2r_g$, then we can write an approximate analytical solution for K_s, the averaged surface curvature, as

$$K_s \sim \sqrt{10}\left(\frac{r_g}{{R_{con}}^2}\right) \tag{C-6}$$

and the length scale in the contact region over which surface diffusion is important, d_s, is given by

$$d_s \sim 0.2 \frac{{R_{con}}^2}{r_g}. \tag{C-7}$$

The grain boundary diffusion sintering mechanism is due to the transport of defects from the interior of a grain along the grain boundary to the contact region and leads to densification (porosity reduction) of the regolith and grain size reduction. The sintering efficiency for the grain boundary mechanism is given by

$$\xi_{GB} = \frac{\gamma_s}{n_0 k T} \delta_{GB} \left(1 - \frac{K_m^2 R_{con}}{2K_s}\right) \tag{C-8}$$

where δ_{GB} is the approximate grain boundary thickness (Goldsby and Kohlstedt, 2001).

Table B.6
Approximate gardening timescales assuming $\rho_{reg} \sim 0.5\rho_{ice}$ corresponding to a 50% porous water ice surface. Orbital distances are given in Saturn radii, R_S. The IDP fluxes were corrected for graviational focusing using recently published IDP fluxes at Saturn (Poppe, 2016), and the yields and E-ring fluxes were taken from Spahn et al. (2006a).

Satellite	Orbital distance [R_s]	Y_{IDP} (10^4)	σ_{IDP} ($\times 10^{-18}$) [g/(cm^2 s)]	σ_{E-ring} ($\times 10^{-15}$) [g/(cm^2 s)]
Mimas	3.08	1.8	2.5	62
Tethys	4.89	1.2	2.0	230
Dione	6.26	0.98	1.6	27

References

Annex, A., Verbiscer, A.J., Helfenstein, P., Howett, C., Schenk, P., 2013. Photometric properties of thermally anomalous terrain on icy saturnian satellites. In: AAS/Division for Planetary Sciences Meeting Abstracts. In: AAS/Division for Planetary Sciences Meeting Abstracts, 45, p. 417.02.

Batchelor, G.K., O'Brien, R.W., 1977. Thermal or electrical conduction through a granular material. R. Soc. London Proc. Series A 355, 313–333.

Blackford, J.R., 2007. Sintering and microstructure of ice: A review. J. Phys. D. Appl. Phys. 40, R355–R385.

Bringa, E.M., Johnson, R.E., 2004. A new model for cosmic-ray ion erosion of volatiles from grains in the interstellar medium. Astrophys. J. 603, 159–164.

Buratti, B.J., Mosher, J.A., Johnson, T.V., 1990. Albedo and color maps of the Saturnian satellites. Icarus 87, 339–357.

Chan, C., Tien, C., 1973. Conductance of packed spheres in vacuum. J. Heat Transfer - Trans. ASME 95 (3), 302–308.

Cooper, J.F., Johnson, R.E., Mauk, B.H., Garrett, H.B., Gehrels, N., 2001. Energetic ion and electron irradiation of the icy Galilean satellites. Icarus 149, 133–159.

Cooper, M., Mikic, B., Yovanovich, M., 1969. Thermal contact conductance. Int. J.Heat and Mass Transfer 12 (3), 279–300.

Cuzzi, J.N., Estrada, P.R., 1998. Compositional evolution of Saturn's rings due to meteoroid bombardment. Icarus 132, 1–35.

Dartois, E., Alata, I., Engrand, C., Brunetto, R., Duprat, J., Pinot, T., Quirico, E., Remusat, L., Bardin, N., Briani, G., Mostefaoui, S., Morinaud, G., Crane, B., Szwec, N., Delauche, L., Jamme, F., Sandt, C., Dumas, P., 2015. Interstellar and interplanetary solids in the laboratory. Bulletin de la Societe Royale des Sciences de Liege 84, 7–14.

Dartois, E., Ding, J.J., de Barros, A.L.F., Boduch, P., Brunetto, R., Chabot, M., Domaracka, A., Godard, M., Lv, X.Y., Mejía Guamán, C.F., Pino, T., Rothard, H., da Silveira, E.F., Thomas, J.C., 2015. Swift heavy ion irradiation of water ice from MeV to GeV energies. Approaching true cosmic ray compaction. Astron. Astrophys. 557, A97.

Dougherty, M.K., Khurana, K.K., Neubauer, F.M., Russell, C.T., Saur, J., Leisner, J.S., Burton, M.E., 2006. Identification of a dynamic atmosphere at Enceladus with the Cassini magnetometer. Science 311, 1406–1409.

Elder, C., Helfenstein, P., Thomas, P., Veverka, J., Burns, J.A., Denk, T., Porco, C., 2007. Tethys' mysterious equatorial band. In: AAS/Division for Planetary Sciences Meeting Abstracts #39. In: Bulletin of the American Astronomical Society, 39, p. 429.

F. Salvat, J. F.-V., Sempau, J., 2011. PENELOPE-2011: A Code System for Monte Carlo Simulation of Electron and Photon Transport. OECD-NEA. Issy-les-Moulineaux, France.

Ferrari, C., Reffet, E., 2013. The dark side of Saturn's B-ring: Seasons as clues to its structure. Icarus 223, 28–39.

Filacchione, G., Capaccioni, F., Clark, R.N., Cuzzi, J.N., Cruikshank, D.P., Coradini, A., Cerroni, P., Nicholson, P.D., McCord, T.B., Brown, R.H., Buratti, B.J., Tosi, F., Nelson, R.M., Jaumann, R., Stephan, K., 2010. Saturn's icy satellites investigated by Cassini-VIMS. II. Results at the end of nominal mission. Icarus 206, 507–523.

Gibson, K.D., Killelea, D.R., Yuan, H., Becker, J.S., Sibener, S.J., 2011. Determination of the sticking coefficient and scattering dynamics of water on ice using molecular beam techniques. J. Chem. Phys. 134 (3). 034703–034703

Goldsby, D.L., Kohlstedt, D.L., 2001. Superplastic deformation of ice: Experimental observations. J. Geophys. Res. 106, 11017.

Gundlach, B., Blum, J., 2012. Outgassing of icy bodies in the Solar System - II: Heat transport in dry, porous surface dust layers. Icarus 219, 618–629.

Hamilton, D.P., Burns, J.A., 1994. Origin of Saturn's E-ring: Self-sustained, naturally. Science 264, 550–553.

Hendrix, A.R., Cassidy, T.A., Buratti, B.J., Paranicas, C., Hansen, C.J., Teolis, B., Roussos, E., Todd Bradley, E., Kollmann, P., Johnson, R.E., 2012. Mimas' far-UV albedo: Spatial variations. Icarus 220, 922–931.

Henry, M., 2003. First-principles derivation of vacuum surface energies from crystal structures. Solid State Sci. 5 (9), 1201–1205.

Hobbs, P., 1974. Ice Physics. Clarendon Press.

Howett, C.J.A., Spencer, J.R., Hurford, T., Verbiscer, A., Segura, M., 2012. PacMan returns: An electron-generated thermal anomaly on Tethys. Icarus 221, 1084–1088.

Howett, C.J.A., Spencer, J.R., Hurford, T., Verbiscer, A., Segura, M., 2014. Thermophysical property variations across Dione and Rhea. Icarus 241, 239–247.

Howett, C.J.A., Spencer, J.R., Schenk, P., Johnson, R.E., Paranicas, C., Hurford, T.A., Verbiscer, A., Segura, M., 2011. A high-amplitude thermal inertia anomaly of probable magnetospheric origin on Saturn's moon Mimas. Icarus 216, 221–226.

Johnson, K.L., Kendall, K., Roberts, A.D., 1971. Surface energy and the contact of elastic solids. R. Soc. London Proc. Series A 324, 301–313.

Johnson, R.E., 1990. Energetic Charged-Particle Interactions with Atmospheres and Surfaces. Physics and Chemistry in Space, 19. Springer-Verlag Berlin Heidelberg.

Johnson, R.E., Liu, M., 1996. Molecular dynamics studies of minicascades in electronically stimulated sputtering of condensed-gas solids. J. Chem. Phys. 104, 6041–6051.

Juhász, A., Horányi, M., 2002. Saturn's E-ring: A dynamical approach. J. Geophys. Res. (Space Physics) 107, 1066.

Kaoumi, D., Motta, A.T., Birtcher, R.C., 2008. A thermal spike model of grain growth under irradiation. J. Appl. Phys. 104 (7), 073525.

Kirchoff, M.R., Schenk, P., 2009. Crater modification and geologic activity in Enceladus' heavily cratered plains: Evidence from the impact crater distribution. Icarus 202, 656–668.

Kouchi, A., Yamamoto, T., Kozasa, T., Kuroda, T., Greenberg, J.M., 1994. Conditions for condensation and preservation of amorphous ice and crystallinity of astrophysical ices. Astron. Astrophys. 290, 1009–1018.

Krimigis, S.M., Mitchell, D.G., Hamilton, D.C., Livi, S., Dandouras, J., Jaskulek, S., Armstrong, T.P., Boldt, J.D., Cheng, A.F., Gloeckler, G., Hayes, J.R., Hsieh, K.C., Ip, W.-H., Keath, E.P., Kirsch, E., Krupp, N., Lanzerotti, L.J., Lundgren, R., Mauk, B.H., McEntire, R.W., Roelof, E.C., Schlemm, C.E., Tossman, B.E., Wilken, B., Williams, D.J., 2004. Magnetosphere imaging instrument (MIMI) on the Cassini mission to Saturn/Titan. Space Sci. Rev. 114, 233–329.

Kuczynski, G., 1972. Physics and chemistry of sintering. Adv. Colloid Interf. Sci. 3 (3), 275–330.

Livingston, F.E., Whipple, G.C., George, S.M., 1998. Surface and bulk diffusion of HDO on ultrathin single-crystal ice multilayers on Ru(001). Journal of Chemical Physics 108, 2197–2207.

Myers, S.M., 1980. Ion-beam-induced migration and its effect on concentration profiles. Nuclear Instrum. Methods 168, 265–274.

Nasello, O.B., Navarro de Juarez, S., Di Prinzio, C.L., 2007. Measurement of self-diffusion on ice surface. Scripta Materialia 56 (12), 1071–1073.

Nelson, R.M., Boryta, M.D., Hapke, B.W., Manatt, K.S., Nebedum, A., Kroner, D., Shkuratov, Y., Psarev, V., Smythe, W.D., 2015. Jupiter's satellite Europa: Evidence for an extremely fine-grained, high porosity surface. In: AAS/Division for Planetary Sciences Meeting Abstracts. In: AAS/Division for Planetary Sciences Meeting Abstracts, 47, p. 405.02.

Nie, S., Bartelt, N.C., Thürmer, K., 2009. Observation of surface self-diffusion on ice. Phys. Rev. Lett. 102 (13), 136101.

Paranicas, C., Carlson, R.W., Johnson, R.E., 2001. Electron bombardment of Europa. Geophys. Res. Lett. 28, 673–676.

Paranicas, C., Roussos, E., Decker, R.B., Johnson, R.E., Hendrix, A.R., Schenk, P., Cassidy, T.A., Dalton, J.B., Howett, C.J.A., Kollmann, P., Patterson, W., Hand, K.P., Nordheim, T.A., Krupp, N., Mitchell, D.G., 2012. The lens feature on the inner Saturnian satellites. Icarus 234, 155–161.

Piqueux, S., Christensen, P.R., 2009. A model of thermal conductivity for planetary soils: 2. Theory for cemented soils. J. Geophys. Res. (Planets) 114, E09006.

Poppe, A.R., 2016. An improved model for interplanetary dust fluxes in the outer Solar System. Icarus 264, 369–386.

Porco, C.C., Helfenstein, P., Thomas, P.C., Ingersoll, A.P., Wisdom, J., West, R., Neukum, G., Denk, T., Wagner, R., Roatsch, T., Kieffer, S., Turtle, E., McEwen, A., Johnson, T.V., Rathbun, J., Veverka, J., Wilson, D., Perry, J., Spitale, J., Brahic, A., Burns, J.A., Del Genio, A.D., Dones, L., Murray, C.D., Squyres, S., 2006. Cassini observes the active south pole of Enceladus. Science 311, 1393–1401.

Porter, S.B., Desch, S.J., Cook, J.C., 2010. Micrometeorite impact annealing of ice in the outer Solar System. Icarus 208, 492–498.

Presley, M.A., Christensen, P.R., 1997. Thermal conductivity measurements of particulate materials 2. Results. J. Geophys. Res. 102, 6551–6566.

Raut, U., Famá, M., Loeffler, M.J., Baragiola, R.A., 2008. Cosmic ray compaction of porous interstellar ices. Astrophys. J. 687, 1070–1074.

Roussos, E., Jones, G.H., Krupp, N., Paranicas, C., Mitchell, D.G., Lagg, A., Woch, J., Motschmann, U., Krimigis, S.M., Dougherty, M.K., 2007. Electron microdiffusion in the Saturnian radiation belts: Cassini MIMI/LEMMS observations of energetic electron absorption by the icy moons. J. Geophys. Res. (Space Physics) 112, A06214.

Schenk, P., Hamilton, D.P., Johnson, R.E., McKinnon, W.B., Paranicas, C., Schmidt, J., Showalter, M.R., 2011. Plasma, plumes and rings: Saturn system dynamics as recorded in global color patterns on its midsize icy satellites. Icarus 211 (1), 740–757.

Scipioni, F., Schenk, P., 2014. Spectroscopic variation of water ice abundance across Mimas and Tethys' surface. In: AAS/Division for Planetary Sciences Meeting Abstracts. In: AAS/Division for Planetary Sciences Meeting Abstracts, 46, pp. 502–503.

Scipioni, F., Schenk, P., Tosi, F., Clark, R., Dalle Ore, C., Combe, J.-P., 2015. Discovering sub-micron ice particles across Dione' surface. In: AAS/Division for Planetary Sciences Meeting Abstracts. In: AAS/Division for Planetary Sciences Meeting Abstracts, 47, p. 508.03.

Shewmon, P., 1963. Diffusion in Solid. McGraw-Hill series in materials science and engineering, McGraw-Hill.

Sigmund, P., 1969. Theory of sputtering. I. Sputtering yield of amorphous and polycrystalline targets. Phys. Rev. 184, 383–416.

Sirono, S.-i., 2011. The sintering region of icy dust aggregates in a protoplanetary nebula. Astrophys. J. 735, 131.

Sirono, S.-i., Yamamoto, T., 1997. Thermal conductivity of granular materials relevant to the thermal evolution of cometary nuclei. Planet. Space Sci. 45, 827–834.

Spahn, F., Albers, N., Hörning, M., Kempf, S., Krivov, A.V., Makuch, M., Schmidt, J., Seiß, M., Miodrag Sremčević, 2006. E-ring dust sources: Implications from Cassini's dust measurements. Planet. Space Sci. 54, 1024–1032.

Spahn, F., Schmidt, J., Albers, N., Hörning, M., Makuch, M., Seiß, M., Kempf, S., Srama, R., Dikarev, V., Helfert, S., Moragas-Klostermeyer, G., Krivov, A.V., Sremčević, M., Tuzzolino, A.J., Economou, T., Grün, E., 2006. Cassini dust measurements at Enceladus and implications for the origin of the E-ring. Science 311, 1416–1418.

Stooke, P.J., 1989. Tethys: Volcanic and structural geology. In: Lunar and Planetary Science Conference. In: Lunar and Planetary Inst. Technical Report, 20, p. 1071.

Stooke, P.J., 2002. Tethys and Dione: New geological interpretations. In: Lunar and Planetary Science Conference. In: Lunar and Planetary Science Conference, 33.

Swinkels, F., Ashby, M., 1981. Overview 11 - A 2nd report on sintering diagrams. Acta Metallurgica 29 (2), 259–281.

Urbassek, H.M., Bradley, R.M., Nietiadi, M.L., Moeller, W., 2015. Sputter yield of curved surfaces. Phys. Rev. B 91 (16), 165418.
Vassiliev, O.N., 2012. Electron slowing-down spectra in water for electron and photon sources calculated with the geant4-dna code. Phys. Med. Biol. 57 (4), 1087.
Verbiscer, A., French, R., Showalter, M., Helfenstein, P., 2007. Enceladus: cosmic graffiti artist caught in the act. Science 315, 815.
Verbiscer, A.J., Helfenstein, P., Howett, C., Annex, A., Schenk, P., 2014. Spectrophotometric properties of thermally anomalous terrain on Mimas. In: AAS/Division for Planetary Sciences Meeting Abstracts. In: AAS/Division for Planetary Sciences Meeting Abstracts, 46, p. 502.08.
Watkins, M., Pan, D., Wang, E.G., Michaelides, A., Vandevondele, J., Slater, B., 2011. Large variation of vacancy formation energies in the surface of crystalline ice. Nat. Mater. 10, 794–798.
Wei, Q., Eddy, M., Li, K.-D., Wang, L., 2009. Influence of surface morphology on sputtering yields. J. Phys. D App. Phys. 42 (16), 165304.
Westley, M.S., Baragiola, R.A., Johnson, R.E., Baratta, G.A., 1995. Photodesorption from low-temperature water ice in interstellar and circumsolar grains. Nature 373, 405–407.
Wood, S.E., 2013a. An Analytic Model for the Thermal Conductivity of Planetary Regolith: Uncemented, Non-Spherical Particulates. In: Lunar and Planetary Science Conference. Vol. 44: Lunar and Planetary Inst. Technical Report, p. 3077.
Wood, S.E., 2013b. Analytic Model for Thermal Conductivity (k_{th}) of Planetary Regolith: Uncemented, Cohesive or Compressed, Non-Spherical Particles. In: Poster presented at the 2013 Lunar and Planetary Science Conference; March 18–22. The Woodlands, TX, p. 3900. E-poster PDF: http://www.lpi.usra.edu/meetings/lpsc2013/eposter/3077.pdf.